EUROFUSION WPJET1-PR(16) 14684

V Riccardo et al.

Power footprint definition for JET dvertor protection

Preprint of Paper to be submitted for publication in
22nd International Conference on Plasma Surface Interactions
in Controlled Fusion Devices (22nd PSI)

This work has been carried out within the framework of the EUROfusion Consortium and has received funding from the Euratom research and training programme 2014-2018 under grant agreement No 633053. The views and opinions expressed herein do not necessarily reflect those of the European Commission.

Power footprint definition for JET divertor protection

V. Riccardo[a], G.F. Matthews[a], I. Balboa[a], T. Eich[b], D. Iglesias[a], S. Silburn[a]
and JET Contributors[c]

EUROfusion Consortium JET, Culham Science Centre, Abingdon, OX14 3DB, UK
[a]*Culham Science Centre, Abingdon, Oxfordshire, OX14 3DB, U.K.*
[b]*Max-Planck-Institut für Plasmaphysik, Boltzmannstr.2, D-85748, Germany*
[c]*Appendix of F. Romanelli et al., Proc. 25th IAEA Fusion Energy Conference 2014, Saint Petersburg, Russia*

valeria.riccardo@ukaea.org

Abstract

Keeping the surface temperature of plasma facing components within allowable limits is important for the operation of JET and will be even more critical in actively cooled machines such as ITER. Protection by direct observation using IR or near IR cameras has its limitations and no predictive capability.
Defining the power footprint as a function of engineering parameters offers the capability to predict target temperatures both during the planning phase and, once integrated in the protection system, in real time. Physics scalings exist for the power scrape-off length, but these have been developed after cleaning all operational 'disturbances'. Some of the physics-based scalings also differentiate between ELM and inter-ELM, whereas for engineering/protection purposes what counts in order to determine peak surface temperature is the average effect of all power loads.
The power footprints, measured using IR cameras in a variety of attached operational conditions, have been fitted with an exponential convoluted with a Gaussian [T. Eich, 2013]. Using this parametrization, developed for the inter-ELM phase, also for the ELM phase, possible non-diffusive effects in the dissipation process are neglected in the analysis. The effects of various 'disturbances' on the fitting parameters have been quantified, resulting in an improved selection of engineering parameters to define the scaling of the effective power footprint.

Keywords: Divertor heat loads, scrape off layer
PACS: 52.70Kz, 52.55Rk, 52.70Ds

1. Introduction

The most likely route to achieve high fusion gain in ITER and beyond is currently H-mode X-point operation. In this scenario, most of the power crossing the separatrix flows inside a narrow channel on open field lines in the scrape-off layer connecting directly to the divertor target plates. Therefore the control of the surface temperature of plasma facing components within allowable limits is critical. Protection by direct observation using IR or near IR cameras has limitations (for example, affected by the condition of the target surface and in certain geometries by reflections, incompatible with the magnetic and/or nuclear environment) and

also has no predictive capability. Defining the power footprint as a function of engineering parameters offers the capability to predict target temperatures. Physics scalings exist for the power scrape-off length. The ITER Physics basis scrape off layer definition [1] is based mostly on JET ELM-averaged data, while other scalings differentiate between ELM and inter-ELM, for example [2] is devoted to an inter-ELM multi-machine study. However, for engineering/protection purposes what counts in order to determine peak surface temperature is the average effect of all power loads.

This paper is based on the analysis of the power footprints, measured using IR cameras in a variety of attached operational conditions, resulting in the definition of a pragmatic power footprint. Two sets of pulses have been analyzed, one from the last years of the carbon divertor and one from the first three years after the installation of the ITER-like Wall (ILW). The same pulses used (and validated) in [2] are used here. The two sets of pulses respectively cover a plasma current range of 1.5-3.5MA and 1.0-3.0MA, a toroidal field range of 1.5-3.2T and 1.0-2.8T, a line-integral density range of 1.0-2.3 10^{20}m^{-2} and 0.7-2.1 10^{20}m^{-2} and SOL power range of 3.4-19.5MW and 3.5-22.2MW. The footprint is analyzed over 0.5s while plasma current, toroidal field, additional power and density are within 5% of their average and the requested strike-point radial position is constant.

The analysis of the IR data is described in Section 2. In Section 3 the effect of various 'disturbances' on the fitting parameters is discussed and quantified. The analysis of the 'disturbances' is then used as a guide in the selection of engineering parameters to define the scaling rule for the fitting parameters. The definition of the engineering profile is presented in Section 4 and discussed in Section 5.

2. IR data analysis

The JET divertor is seen from the top by two IR cameras and from the side by a third one [3]. The data from one on the vertical viewing cameras (KL9B) is used in this analysis. The IR camera measures light intensity, which is converted into temperature according to the camera calibration. The power density is calculated from the temperature using a 1D thermal code, Theodor [4]. This process can be prone to inaccuracies (calibration uncertainties, simplification in the 1D model, etc). In this analysis the objective is the definition of the shape, along the radial direction, of the power density profile; this is fairly robust to calibration uncertainties, but can be affected by simplifications in the thermal model (for example negative heat loads and in the ILW layout edge discontinuities). Averaging the power density profiles over a certain time interval can reduce some uncertainties.

The power density profiles calculated from the tile surface temperature measured by the IR camera on the outer target (which in the following will be referred to as "measured profiles") have been fitted with an exponential convoluted with a Gaussian [2].

$$q(R) = \frac{q_0}{2}\exp\left(\left(\frac{S}{2\lambda}\right)^2 - \frac{R-R_{SP}}{\lambda}\right)\operatorname{erfc}\left(\frac{S}{2\lambda} - \frac{R-R_{SP}}{S}\right) + q_b \qquad (1)$$

The free parameters to fit the power density profile are the decay length of the exponent, λ, the standard deviation of the Gaussian, S, the background power density, q_b, the shaped power density, q_0, and the position of the peak, R_{SP} (strike point). This fit has been developed for inter-ELM, however it works on time averaged profiles including the ELM phase as the relative amount of energy deposited by the ELMs is small.

Profiles can be fitted for each time step or as average of selected time windows. A successful fit, or convergence, is achieved when the error is within the target for the maximum allowed number of attempts for at least one of the nine suggested strike point positions. The single time step fit is not always successful: fitting is especially unlikely near ELMs because the shape of the power density profile of ELMs is rather different from the shape of the power density profile between ELMs and ELM-averaged. For some ILW pulses also the time averaged fit is not possible due to the effect of the geometrical discontinuity on the solution of the thermal model.

The IR profiles have been fitted at each time step for a number of pulses, one example is shown in Fig. 1. Here the fitting parameters are plotted together with the D_α light in the outer divertor, which has a spike at the time of the ELM, the current in the radial field circuit, used to control the vertical position of the plasma, and the position of the peak in the measured IR profile. Consistently with previous observations [5], after an ELM the position of the strike point moves outboard (positive dR_{fit}). Later the strike point moves back to the pre-ELM position. While the movement just after the ELM is not linked to the control system (current in the radial field circuit), the return to the nominal position is. In the subset of pulses where profiles have been fitted at each time step, there is good agreement between the position of the peak of the IR measured and fitted profile. The Gaussian standard deviation, S, and the decay length of the exponential, λ, factors of the power density profile tend to be larger after an ELM than before. During the inter-ELM phase the profile peaking increases while approaching an ELM. The background power density, q_b, is significant only shortly after ELMs.

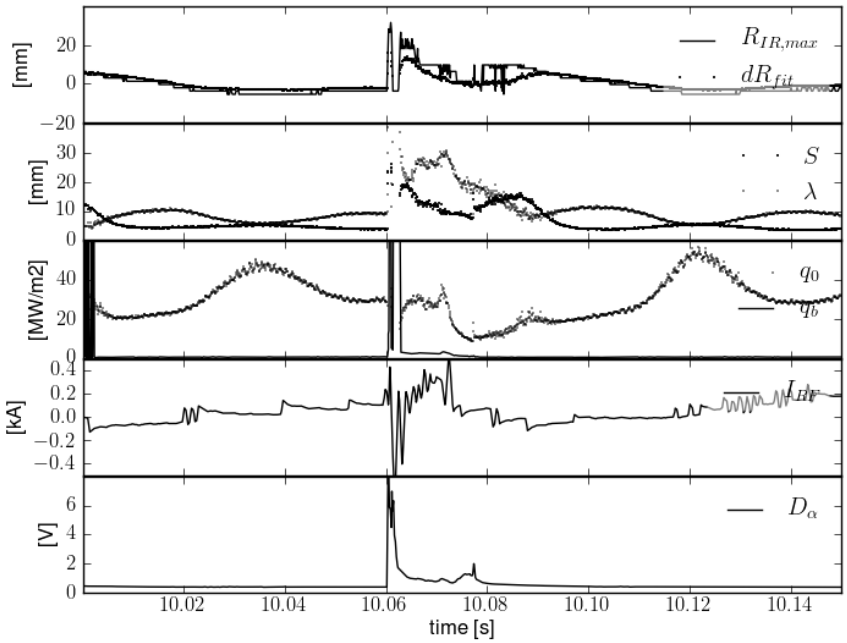

Fig. 1 Pulse 79684: $R_{IR,max}$ is the position of the peak of the measured IR power density profile with respect to its average over the time window. dR_{fit} is the position of the peak of the fitted power density profile with respect to its average over the time window. S, λ, q_0, and q_b are the parameters fitted to the IR power density profile at each time step. I_{RF} is the current in the radial field circuit. D_α (light in the outer divertor) is a measure of the ELMs.

3. Analysis of 'disturbances'

The broadening of the power density profile can be due to both the change in profile shape caused by ELMs and the strike point movement. In order to be able to remove the effect of the strike point movement, the converged fitted profiles can be used to create four types of time-averaged profiles:

- Average of all converged profiles in their original strike point position
- Average of non-ELM converged profiles in their original strike point position
- Average of all converged profiles shifted to the mean strike point position
- Average of non-ELM converged profiles shifted to the mean strike point position

The non-ELM condition is determined as a function of the D_α signal: when this is above a set fraction of the peak the ELM phase starts; the ELM phase ends when the D_α signal returns to a value lower than 10 time steps before the start of the ELM phase. In this exercise some ELM broadening is lost as the profile during the ELM are the least likely to have converged.

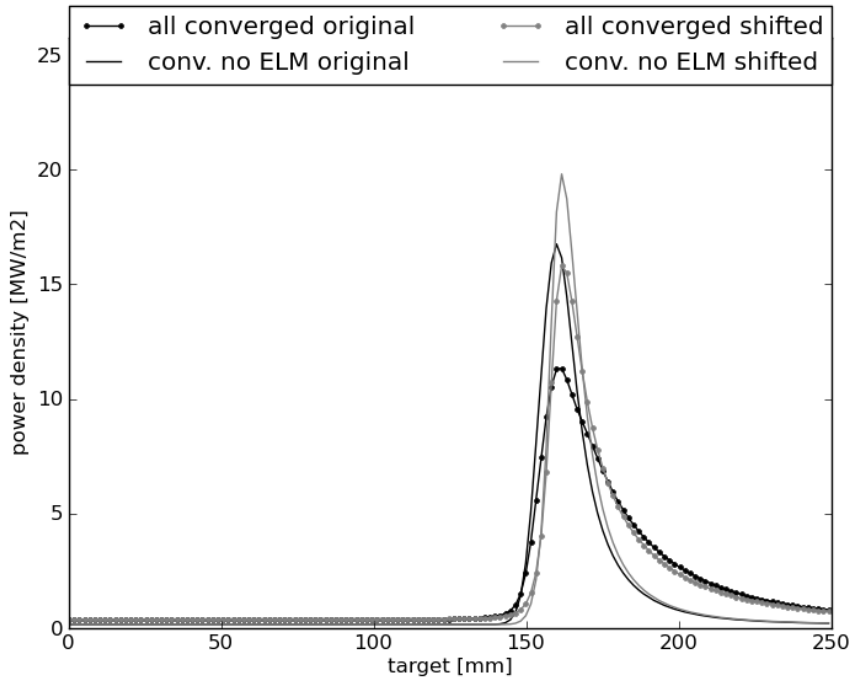

Fig. 2 Fit to profiles averaged over different types of time samples for a C-wall pulse (79684 between 13.s and 13.5s).

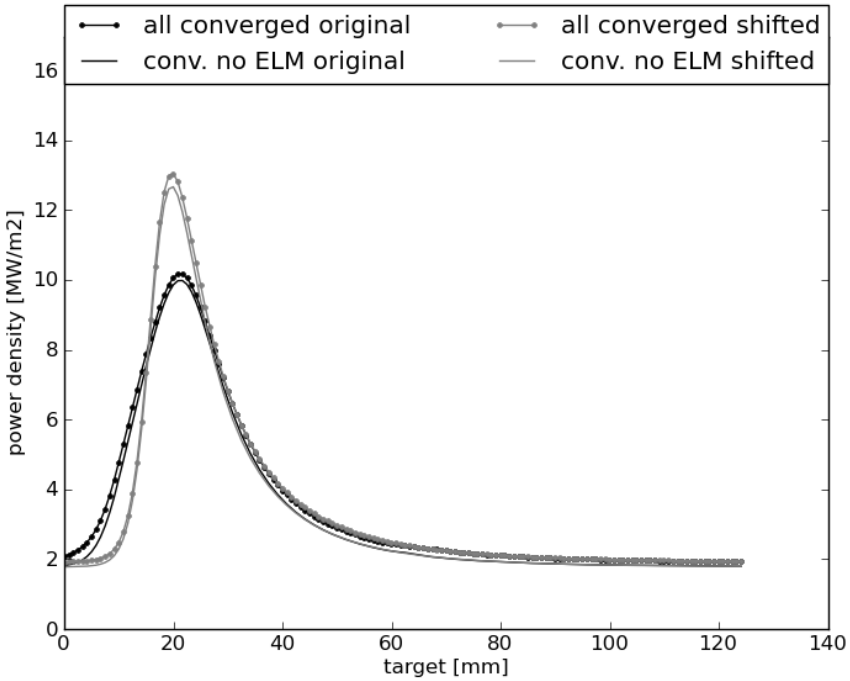

Fig. 3 Fit to profiles averaged over different types of time samples for an ILW pulse (82643 between 15.s and 15.5s). The W target is made of 4 lamellae covering the same length as the carbon tile, only the outer two lamellae are used in this analysis.

	79684		**82643**	
Measured at target	**λ [mm]**	**S [mm]**	**λ [mm]**	**S [mm]**
Converged + original	23.7	5.9	10.8	8.1
No ELM + original	9.4	5.7	10.5	7.8
Converged + shifted	16.0	4.0	11.0	4.0
No ELM + shifted	8.8	4.1	10.3	4.0
Overall average	24.2	5.5	15.8	8.5
Single inter-ELM (Fig.1 in [2])	7.2	4.0		

Table 1 Fit parameters computed for profiles averaged over different types of time samples for a C-wall pulse (79684) and an ILW pulse (82643). The single ELM data: midplane λ 1.26mm, midplane S=0.70mm, flux expansion 5.72.

Two pulses, one from the C-wall subset and one from the ILW subset are reported in Fig. 2 and Fig. 3 respectively. The total number of time samples for the C-wall pulse (79684) is 9985; of these 8321 converged and 4575 were away from ELM phases. The total number of time samples for the ILW pulse (82643) is 9986; of these 8385 converged and 7897 were away from

ELM phases. The ELM behavior is significantly different in the two pulses. The C-wall pulse has few, very large type-I ELMs, with the D_α signal remaining large for several ms after peaking. The ILW pulse has several smaller ELMs, with the D_α signal returning to pre-ELM values promptly. This explains the difference in number of non-ELM time points. In the C-wall pulse, the strike point position moves relatively more but far less often than in the ILW pulse. In the ILW pulse there is a clear difference between the average profile taken with the original (moving) strike point and the average profile taken with the shifted strike point (stationary), while the effect of the ELM is minimal: the no-ELM profiles nearly overlap the unfiltered profiles. In the C-wall pulses there is also a clear difference between the average profile taken with the original strike point and the average profile taken with the shifted strike point, but there is also a significant difference between the unfiltered and the no-ELM profiles, with the profiles including the ELM phase much broader than those excluding the ELM phase. The difference in the ELM effect on the two pulses is due to the difference in the ELM behavior between the C-wall and the ILW (in the ILW infrequent large ELMs are hardly attainable) and the difficulties in fitting ELM profiles on the ILW target, so most of the ELM contribution has been lost. For these two pulses the key fitting parameters are summarized in Table 1. Here, as well as the fitting λ and S for the four types of average profiles also the fitting λ and S for the overall average profile is included for both pulses and the inter-ELM single fit is added from Fig. 1 of [2] only for the C-wall case. There is good agreement between the "No ELM + shifted" and the inter-ELM single, demonstrating consistency with previous analyses. The overall average profile takes into account also non-converged ELM profiles, as the profile to be fitted is taken directly from the profiles calculated from the IR measurements. The fitting parameters for the overall average in the C-wall pulse are in good agreement with those for the average of all the converged profiles. Instead, the fitting parameters for the overall average of the ILW pulse are substantially different from those for the average of all the converged profiles, despite the number of time points failing convergence is much smaller in the ILW pulse than the C-wall pulse, implying that the weight of the non-converged time points in the ILW pulse is high, which is consistent with them belonging to the ELM phase.
The key message to take from Table 1 is that the broadening due to the movement of the strike point strongly affects S but only affect λ when ELMs are included and that the ELM broadening does not affect S, but only affects λ.

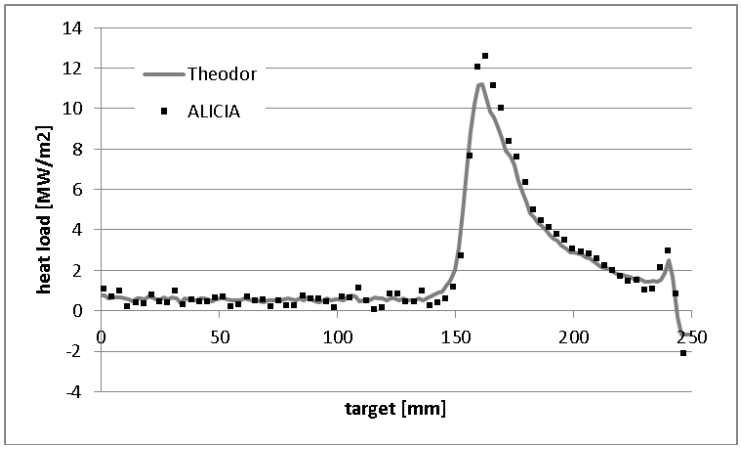

Fig. 4 Comparison of heat load profiles, average between 13.s and 13.5s, for pulse 79684 using Theodor and ALICIA

For one C-wall pulse the average heat load computed using Theodor has been compared with that computed using a different inverse thermal code, ALICIA [6], using temperature dependent thermal properties. Although the ALICIA profile is slightly more peaked, the two profiles are in sufficiently good agreement, as shown in Fig. 4, to give confidence in the Theodor data.

4. Engineering profile

In order to be able to compare the profiles of different magnetic configurations, the quantities measured at the target need to be projected to the outer midplane. The flux expansion 2.5mm outside the separatrix at the outer midplane is taken, as in [2]. The flux expansion is not constant along the target, but the width of the profile is small enough to make the variation over the profile a negligible perturbation on the results.

As the strike point movement is a significant contributor to the broadening of the profile, parameters representing it need to be taken into account. Away from the ELM-phase, the variation of the radial field current is well correlated with the strike point movement (see Fig. 1). Indeed, plotting the midplane λ and S against the standard deviation of the radial field current, shows a linear dependence, Fig. 5 and Fig. 6. To account for the ELM broadening, the ELM frequency has also been included in the pulse parameters. The form of the scaling law chosen is:

$$C_1 {I_p}^a {B_t}^b {n_e}^c {P_{SOL}}^d {f_{ELM}}^e + C_2 \sigma_{RF} \qquad (2)$$

All the quantities are averaged over the analysis time window. I_p is the plasma current in MA, B_t is the toroidal field at the plasma axis in T, n_e is the line integrated density (along a vertical through the centre of the plasma) in 10^{20}m^{-2}, P_{SOL} is the power in the scrape off layer in MW, f_{ELM} is the ELM frequency and σ_{RF} is the standard deviation of the radial field current. The results for the regressions for the midplane λ and S, both in mm, are reported in Table 2. The comparison between measured and calculated midplane λ and S is shown in Fig. 7 and Fig. 8 respectively.

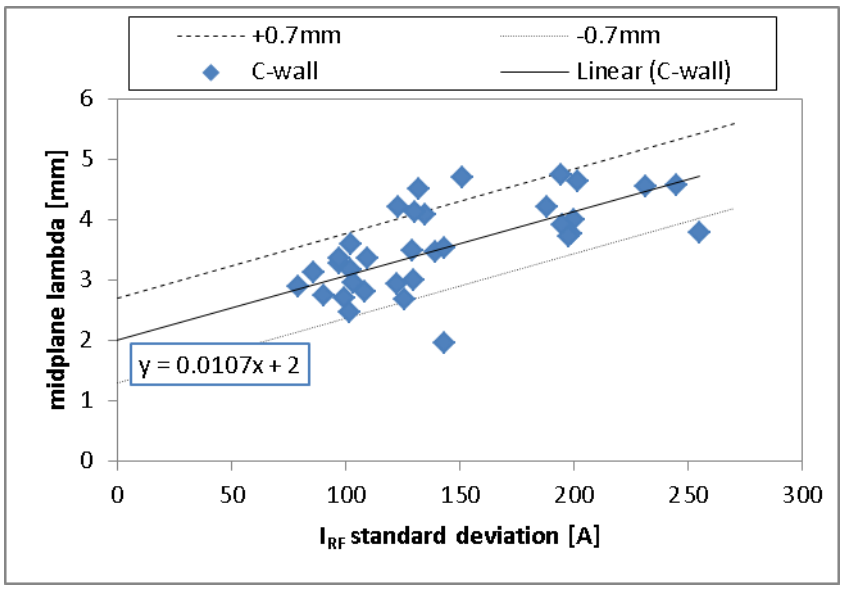

Fig. 5 Dependence of λ on the standard deviation of the radial field current.

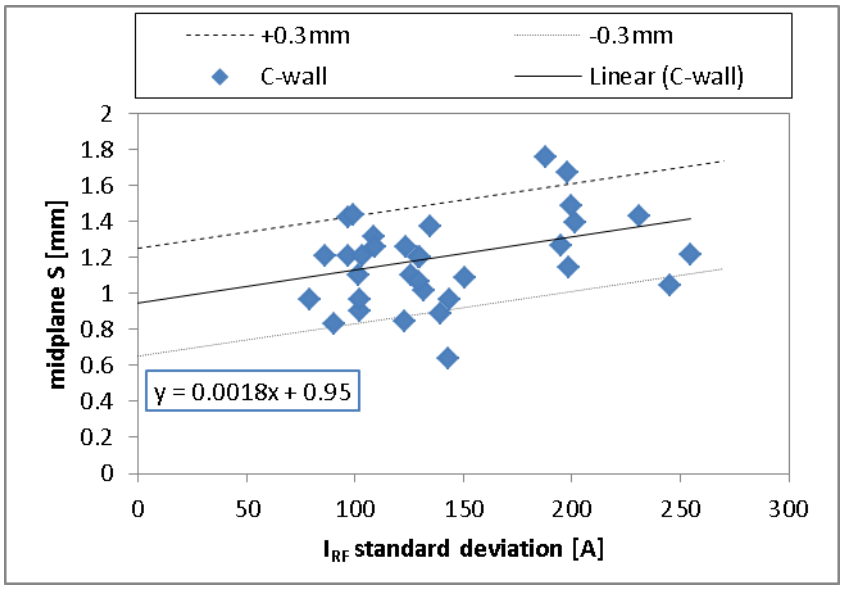

Fig. 6 Dependence of *S* on the standard deviation of the radial field current.

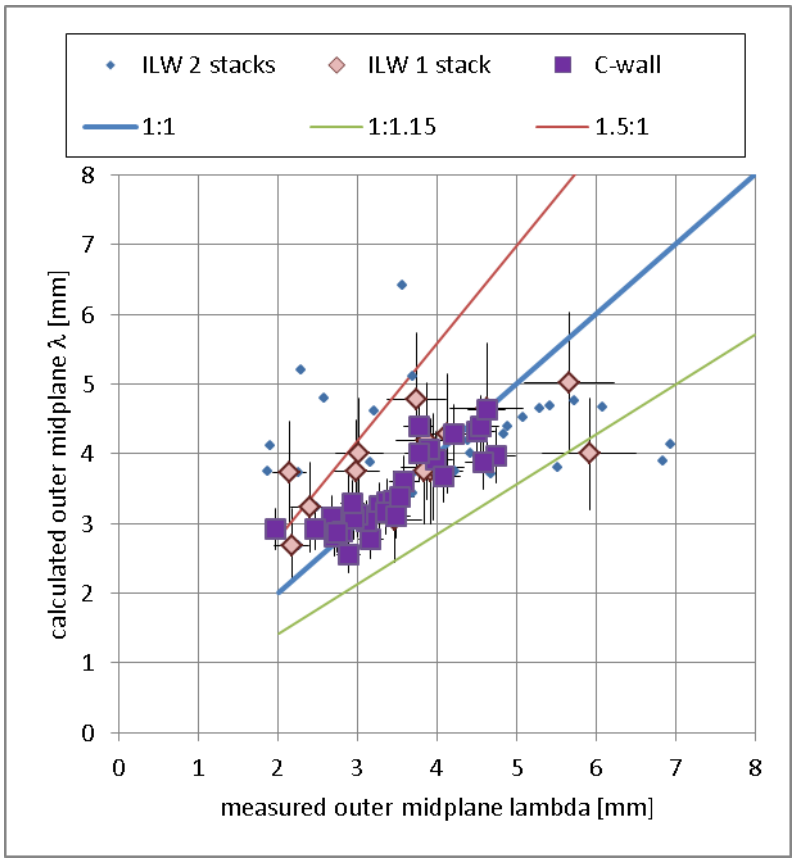

Fig. 7 Comparison between calculated and measured midplane λ.

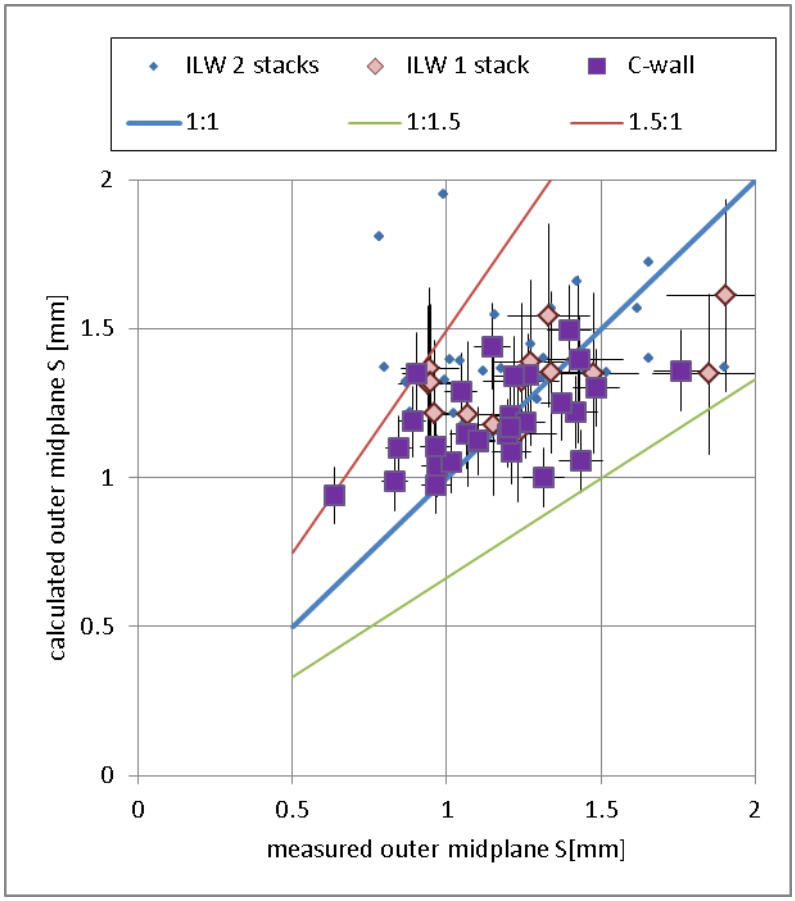

Fig. 8 Comparison between calculated and measured midplane *S*.

		C_1	a	b	c	d	e	C_2
C-wall	λ	1.74	-0.24	0.52	-1.0	0.023	0.054	0.011
	S	0.82	0.74	-0.83	-0.60	0.052	0.084	0.002
ILW	λ	1.6	-0.24	0.52	-1.0	0.023	0.15	0.006
	S	1.6	0.74	-0.83	-0.60	0.052	-0.11	0.002

Table 2 Regression results for the midplane profile λ and *S*.

5. Discussion

Measured and calculated midplane λ and *S* are within a factor of 1.5. For practical applications:

- midplane λ [mm] = $\min(C_{1,\lambda} {I_p}^{a_\lambda} {B_t}^{b_\lambda} {n_e}^{c_\lambda} {P_{SOL}}^{d_\lambda} {f_{ELM}}^{e_\lambda} + C_{2,\lambda}\sigma_{RF}, 2.0)$
- midplane *S* [mm] = $\min(C_{1,S} {I_p}^{a_S} {B_t}^{b_S} {n_e}^{c_S} {P_{SOL}}^{d_S} {f_{ELM}}^{e_S} + C_{2,s}\sigma_{RF}, 0.5)$

The target λ and *S* are obtained multiplying the midplane λ and *S* by the flux expansion extrapolated for the strike point position. Measures from which the input quantities can be calculated are available in real time, although some processing will be necessary.
The different ELM behaviour between C-wall and ILW is accounted for by small changes in the fitting parameters for ELM frequency and radial field standard variation. On average the strike point movement contributes to between 43% (C-wall) and 40% (ILW) of the midplane λ and to between 22% (C-wall) and 36% (ILW) of the midplane *S*.
In the pulse set analyzed, toroidal field, line integrated density and net power tend to scale with plasma current. So the rest of the contributions could be reduced to a plasma current dependency, with $\lambda \sim I_p^{-0.7}$. This is within the range of the regressions in [2] and [7]: $\lambda \sim I_p^{-(0.39\ldots0.99)}$.

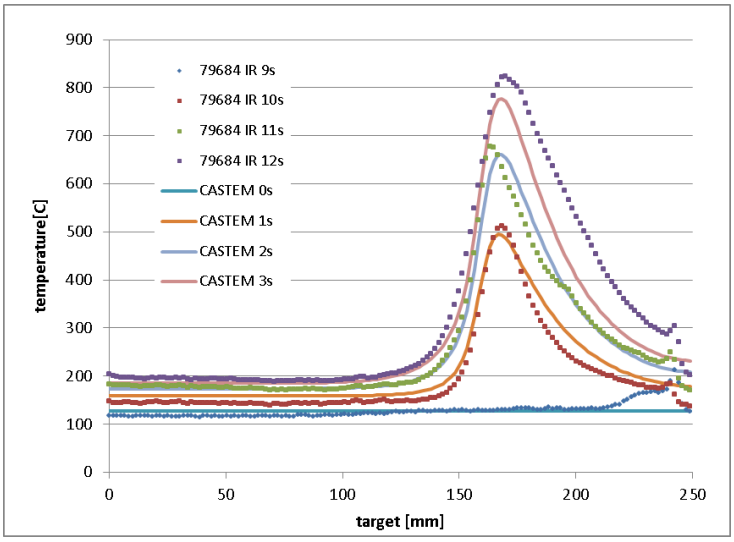

Fig. 9 Comparison between measured and calculated (using "all converged + original" of Fig. 2) surface temperature for pulse 79684.

The main difference between this analysis and analyses like [2] is that the effect of disturbances is taken into account. Disturbances results in a much reduced peak power density see Fig. 2 for example. Using the "all converged + original" heat load of Fig. 2 in a 2D model of the target tile with non-linear thermal properties [8], the surface temperature measured by IR can be reasonably reproduced, as shown in Fig. 9. However, if the "converged + shifted" was used the peak temperature increase over 3s would have been 861°C instead of 649°C, and using the "no ELM + shifted" 1210°C.
The wobbling of the strike point is unavoidable in JET and can be characterized using the radial field current. How much the strike point will wobble in future devises is not predictable, but it is unlikely to be avoidable and it will contribute to the reduction of the effective power density while in attached operation.
Apart from having developed a recipe for the real time definition of the power footprint, a key message resulting from this analysis is that, by taking advantage of the 'disturbances' in the power deposition (ELM spreading and wobbling), more favorable scaling than inter-ELM footprint can be developed for high performance applications.

Acknowledgement

This work has been carried out within the framework of the EUROfusion Consortium and has received funding from the Euratom research and training programme 2014-2018 under grant agreement No 633053. The views and opinions expressed may not reflect those of the European Commission.

References

[1] Progress in the ITER Physics Basis 2007 Nucl. Fusion 47 S203
[2] T. Eich et al, Nucl. Fusion 53 (2013) 093031
[3] I. Balboa et al., Review of Scientific Instruments 83 (2012) 10D530
[4] A. Herrmann et al., Plasma Physics and Controlled Fusion, 37 (1995), 17
[5] E. Solano et al., Nucl. Fusion 48 (2008) 065005
[6] D. Iglesias et al., Virtual prototyping tools for the JET divertor, to be presented at SOFT 2016
[7] R.J. Goldston, Nucl. Fusion 52 (2012) 013009
[8] CEA, DEN, DM2S, SEMT, Cast3M, (http://cast3m.cea.fr/)